

Article

# Engineering Mesoporous NiO with Enriched Electrophilic Ni<sup>3+</sup> and O<sup>-</sup> toward Efficient Oxygen Evolution

Xiu Liu <sup>1,2,3</sup>, Zhi-Yuan Zhai <sup>1</sup>, Zhou Chen <sup>1</sup>, Li-Zhong Zhang <sup>2,\*</sup>, Xiu-Feng Zhao <sup>2</sup>, Feng-Zhan Si <sup>3,\*</sup> and Jian-Hui Li <sup>1,\*</sup>

<sup>1</sup> National Engineering Laboratory for Green Chemical Productions of Alcohols-Ethers-Esters, College of Chemistry and Chemical Engineering, Xiamen University, Xiamen 361005, China; guoguo11266@163.com (X.L.); jz@xmu.edu.cn (Z.-Y.Z.); zc7@ualberta.ca (Z.C.)

<sup>2</sup> Department of Chemistry and Applied Chemistry, Changji University, Changji 831100, China; zhaoxiufeng19670@126.com

<sup>3</sup> College of Materials Science and Engineering, Shenzhen University, Shenzhen 518060, China

\* Correspondence: lzzhang@cjc.edu.cn (L.-Z.Z.); sifengzhan@szu.edu.cn (F.-Z.S.); jhli@xmu.edu.cn (J.-H.L.); Tel.: +86-592-2184591 (J.-H.L.)

Received: 29 June 2018; Accepted: 26 July 2018; Published: 30 July 2018



**Abstract:** Tremendous efforts have been devoted to develop low-cost and highly active electrocatalysts for oxygen evolution reaction (OER). Here, we report the synthesis of mesoporous nickel oxide by the template method and its application in the title reaction. The as-prepared mesoporous NiO possesses a large surface area, uniform mesopores, and rich surface electrophilic Ni<sup>3+</sup> and O<sup>-</sup> species. The overpotential of *meso*-NiO in alkaline medium is 132 mV at 10 mA cm<sup>-1</sup> and 410 mV at 50 mA cm<sup>-1</sup>, which is much smaller than that of the other types of NiO samples. The improvement in the OER activity can be ascribed to the synergy of the large surface area and uniform mesopores for better mass transfer and high density of Ni<sup>3+</sup> and O<sup>-</sup> species favoring the nucleophilic attack by OH<sup>-</sup> to form a NiOOH intermediate. The reaction process and the role of electrophilic Ni<sup>3+</sup> and O<sup>-</sup> were discussed in detail. This results are more conducive to the electrochemical decomposition of water to produce hydrogen fuel as a clean and renewable energy.

**Keywords:** oxygen evolution reaction; mesoporous NiO; water splitting; nucleophilic attack; electrophilic Ni<sup>3+</sup> and O<sup>-</sup>

## 1. Introduction

Nowadays, since clean energy is playing an increasingly important role in environmental protection, hydrogen production by water decomposition has been a hot research topic all along [1]. The research and development of catalysts with high activity and stability has important theoretical significance [2] and application value in the fields of renewable resources for hydrogen production by electrolysis. Hydrogen evolution reaction (HER) and oxygen evolution reaction (OER) are the two half-reactions in electrochemical water that split to produce hydrogen. The OER process has slow reaction dynamics, which consume much more energy in practical applications, and has attracted a great amount of attention from researchers. Currently, the most widely used and efficient catalysts for OER are RuO<sub>2</sub> and IrO<sub>2</sub>. However, these catalysts are scarce in resources and are also expensive, which impeded the large-scale application for commercial purpose. Therefore, in order to overcome these difficulties, it is our goal to develop advanced catalysts with high-stability and low-cost. The studies on first-transition metals, especially Mn, Fe, Co, and Ni-based materials have a growth spurt owing to the good OER performance approaching that of noble metals.

It has been found that in addition to Pt, Pd, and other precious metals, nickel-based electrocatalysts have emerged as outstanding OER catalysts owing to their low price, stability in alkaline solution, relatively low overpotential, and ease of being doped or modified with guest elements. For example, Ni-Fe-CNTs [3] and  $\text{Co}_x\text{Ni}_y\text{S}_z$  [4] octahedral nanocages showed the overpotential of 247 mV and 362 mV at  $10 \text{ mA cm}^{-2}$ , respectively. Among them, NiO is easily available, and possesses a high specific capacitance that is suitable in electrochemical reaction. It was reported that a NiO/Ni heterojunction [5] showed highlighted performance, with the overpotential reaching 1.5 V (versus Reversible Hydrogen Electrode, RHE) at  $20 \text{ mA cm}^{-2}$ . It was reported that the Ni-Co oxide hierarchical nanosheets with a  $\text{Ni}^{3+}$  rich surface benefits the formation of NiOOH, which promotes the OER as the main active site [6].

Since electrochemical processes with electron gain or loss are interfacial phenomena, the electrode materials should possess a high specific surface area with a suitable pore size distribution to enhance the charge-storage capability. The activity of a catalyst depends in part on its surface area [7]. Thus, mesoporous morphology is one of the most important design parameters for making an electrode material. Recently, the synthesis of metal oxide porous electrodes was greatly reported. Compared with micro or macroporous materials, mesoporous materials have unique advantages, such as the larger mesopores increase the internal transmission efficiency of electrons, facilitate contact with active sites, are stable in alkaline solution, have a pore size that is adjustable to control better selectivity, and have a regular pore structure for particles in the rapid proliferation of channels [8]. It is well known that mesopores with sizes in the range of 2 nm to 50 nm are highly desirable for electrochemical reactions, since the mesopores facilitate ionic motion easily. There have been a lot of reports using mesoporous first-transition metal oxides in electrochemical processes, especially in supercapacitors [9–12] and rechargeable batteries [13]. Mesoporous NiO [14] possessed a high surface area, good surface redox reactivity, and consequently a high capacitance of  $124 \text{ F g}^{-1}$ . The mesoporous structure provides  $\text{OH}^-$  accessible pores and a very high surface area ( $477.7 \text{ m}^2 \text{ g}^{-1}$  when calcined at  $250 \text{ }^\circ\text{C}$ ) for charge storage. However, few attempts have been made to employ mesoporous NiO in OER reactions.

The oxygen species and lattice defects for transitional metal oxide may play an important role in electrochemical reactions. However, the role of  $\text{Ni}^{3+}$  in the title reaction has been well recognized, but the effect of oxygen species, especially the electrophilic  $\text{O}^-$  active species, has been rarely studied. In our previous work [15], we have reported that the mesoporous NiO prepared by a surfactant-assisted route allowed efficient molecular transport by diffusion in the channels during the oxidative dehydrogenation of propane reaction. The density of  $\text{Ni}^{3+}$  and  $\text{O}^-$  species are much higher for this mesoporous NiO than for other kinds of NiO. In this work, the same mesoporous nickel oxide with rich  $\text{Ni}^{3+}$  and  $\text{O}^-$  species was synthesized and tested in the oxygen evolution reaction. For comparison, the conventional nano-sized NiO sample was synthesized by a modified sol-gel method. The role of electrophilic  $\text{Ni}^{3+}$  and  $\text{O}^-$  species in the formation of active NiOOH intermediate was fully discussed.

## 2. Results and Discussion

### 2.1. Texture Characterizations

The mesoporous nickel oxide was prepared by a surfactant-templated method via urea hydrolysis of metal nitrates followed by calcination in air, and denoted as *meso*-NiO. For comparison, the traditional nano-sized NiO without the mesoporous structure was prepared by a modified sol-gel method [16] using citric acid as the ligand, and denoted as *bulk*-NiO. The mesoporous structure and surface properties of nickel oxide were characterized by XRD,  $\text{N}_2$  physical adsorption,  $\text{O}_2$  temperature programmed desorption ( $\text{O}_2$ -TPD), X-ray photoelectron spectroscopy (XPS) techniques, and laser Raman spectroscopy. From the XRD patterns shown in Figure 1a, their corresponding XRD patterns indicated the information of pure NiO phase for both samples. The characteristic peaks (111), (200), and (220) can be observed at approximately  $2\theta$  of  $27^\circ$ ,  $43^\circ$ , and  $63^\circ$ . The crystal diffraction for *meso*-NiO is much wider, indicating that the crystallite size for this mesoporous sample is smaller. By the Scherrer

formula ( $L = 0.89\lambda/\beta\cos\theta$ , where  $\beta$  is the half height of the diffraction line,  $\lambda$  is the wavelength, and  $k$  is the diffraction angle), the calculated crystallite size for *meso*-NiO is only 2.1 nm, which is much smaller than the *bulk*-NiO of 17.4 nm. The homogeneous precipitation with surfactant-assisted urea hydrolysis can ensure the smaller crystal size of the NiO catalyst [15].

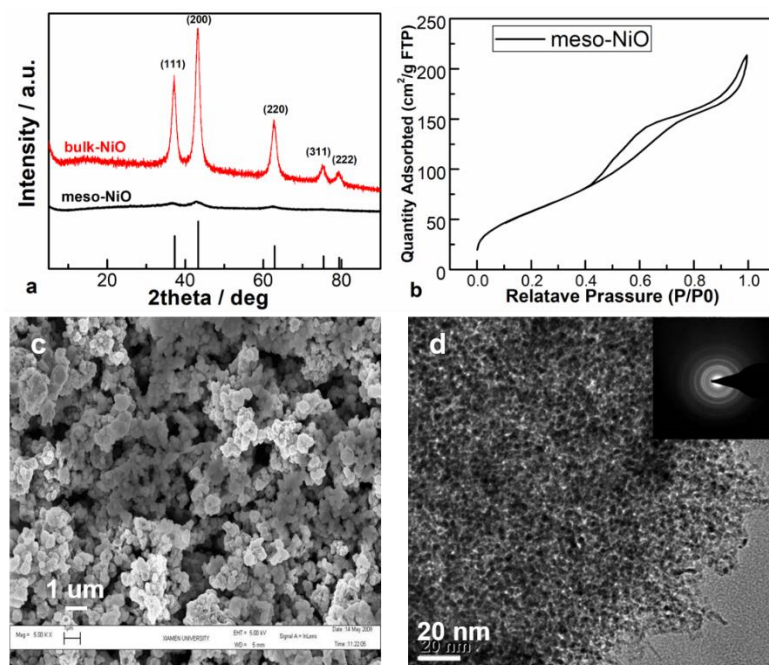


**Figure 1.** (a) XRD pattern of mesoporous nickel oxide and nano-NiO catalysts. (b) Pore size distribution plot of the *meso*-NiO; (c) SEM and (d) TEM images of the *meso*-NiO.

$N_2$  adsorption tests were used to analyze the surface area and pore size distribution. As shown in Figure 1b, the  $N_2$  sorption isotherm shows a type-IV adsorption–desorption behavior with a well-defined pore-filling step at 0.45  $P/P_0$ , indicating the presence of mesopores for the *meso*-NiO sample. The mesoporous size distributions based on the Barrett–Joyner–Halenda (BJH) method are confirmed by the corresponding pore size distribution curves. The Brunauer–Emmett–Teller (BET) specific area is 220.8  $m^2/g$  and 45.3  $m^2/g$  for *meso*-NiO and *bulk*-NiO samples, respectively. The pore size and volume of *meso*-NiO are much larger than that of the *bulk*-NiO. In electrochemistry, a smaller particle size distribution and larger specific surface area will be more beneficial to the improvement of the catalytic efficiency, thereby enhancing the electrochemical activity [17].

The macroscopic pore and mesopore for the *meso*-NiO can be seen from SEM and TEM images, as shown in Figure 1c,d. The macroscopic pore was formed by the aggregations of large particulates, which processes the average size of about 1  $\mu m$  (SEM, Figure 1c). The mesopores were wormhole-like and randomly arranging (TEM, Figure 1d), but the pore sizes were distributed homogeneously within the whole NiO nanoparticles. These wormhole-like pores were formed between NiO nanoparticles due to their aggregation. Unlike  $SiO_2$ , NiO could not form a space-stable ordered structure, because it has a low framework cross-linking and a very strong Ni–O–Ni bond angle, so the stability of the nickel oxide-ordered mesoporous structure is relatively difficult to obtain. Hence, during the electrochemical process, the formation of a wormhole structure allows the electrolyte solution to penetrate and release gases very quickly [18], which can improve the mass transfer and enhance the electrocatalytic activity.

## 2.2. OER Activity

The OER catalytic activities of *meso*-NiO and *bulk*-NiO were tested using a typical three-electrode system in 1.0 M of KOH electrolyte. The samples were deposited onto glassy carbon electrodes to

prepare the working electrodes. Figure 2a,b displays the linear scanning voltammetry (LSV) polarization and Tafel slope curves of *meso*-NiO and *bulk*-NiO with IR-compensation. Obvious oxidation peaks are obtained for *meso*-NiO near 380 mV (versus Ag/AgCl), which represents the oxidation of Ni (II) to Ni (III) [19,20]. Obviously, the specific current density of *meso*-NiO is indeed higher than that of *bulk*-NiO under a certain applied voltage. *Meso*-NiO also presents a slightly earlier onset potential. The overpotentials at  $50 \text{ mA cm}^{-2}$  are 410 mV and 494 mV for *meso*-NiO and *bulk*-NiO, respectively. It is noted that the overpotential at  $10 \text{ mA cm}^{-2}$  is only 132 mV for *meso*-NiO, but it is obtained from the anodic oxidation process, which leads to an unstable potential with running time. Moreover, the corresponding Tafel plots ( $\eta$  versus  $\log(j)$ ) were drawn to study the OER kinetics (Figure 2b). The linear region of the plots is fitted to the equation ( $\eta = a + b \log |j|$ ) yielding the Tafel plots of  $192 \text{ mV dec}^{-1}$  and  $230 \text{ mV dec}^{-1}$  for *meso*-NiO and *bulk*-NiO, respectively. Both Tafel slope values are comparable with the values reported in Zhou's work, where the values are between  $159\text{--}503 \text{ mV dec}^{-1}$ , depending on the different catalysts [21]. Since the Tafel slope is directly associated with the reaction kinetics of an electrocatalyst, the reduced Tafel slope for *meso*-NiO means smaller overpotential changes [22,23], resulting in a faster reaction rate constant, which implies better electrocatalytic kinetics for OER as compared with *bulk*-NiO.

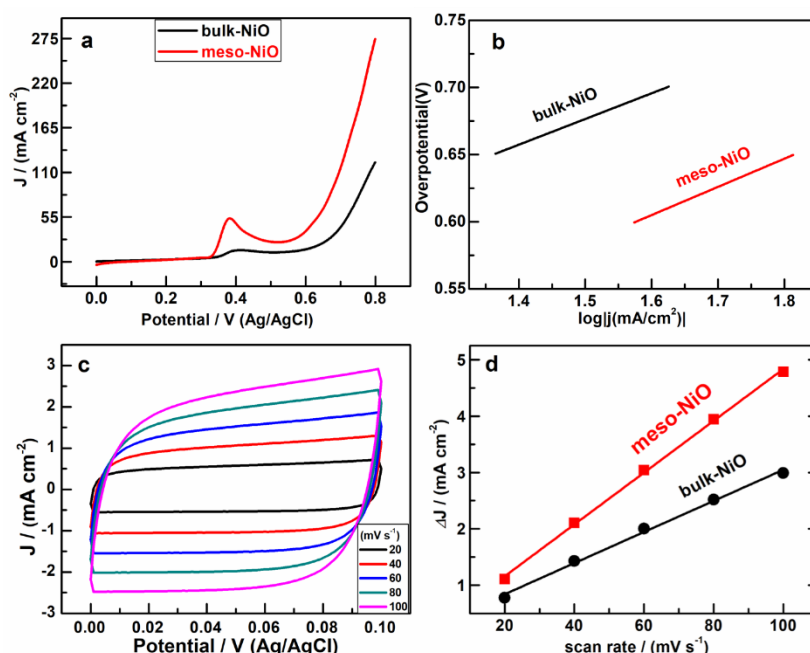


**Figure 2.** (a) Linear scanning voltammetry (LSV) curves over *meso*-NiO and *bulk*-NiO; (b) The corresponding Tafel curves; (c) Cyclic voltammetry scans over *meso*-NiO with different scan rates; (d) Electrochemically active surface area estimated by double-layer capacitance measurements.

The roughness factor (RF) is used to determine the ratio of the electrochemically active surface areas (ECSA) to the geometric surface area of the electrode. To understand the origin of the better OER activity of *meso*-NiO in comparison with *bulk*-NiO and estimate the ECSA and RF, we measured the double-layer capacitance ( $C_{dl}$ ) via a simple cyclic voltammetry (CV) method in a non-Faradaic region at different scan rates [24], as can be seen from the CV curves recorded at different scan rates in Figure 2c. *Meso*-NiO has a larger current density when the scan rate was the same. As demonstrated in Figure 2d, the  $C_{dl}$  of *meso*-NiO ( $23.0 \text{ mF/cm}^2$ ) was higher than that of *bulk*-NiO ( $8.9 \text{ mF/cm}^2$ ), especially when the scan rate was high. This indicated that *meso*-NiO had a greatly increased active site and higher efficient mass and charge transport capability due to the high density of mesopores in the bulk of *meso*-NiO. The larger ECSA values and more active sites can contribute to the better OER electrocatalytic performance. It is important to note that the different catalytic activity has relevance to

the morphology. It seems that the lower overpotential of *meso*-NiO than that of *bulk*-NiO results from the better intrinsic activity of *meso*-NiO than *bulk*-NiO for OER under alkaline condition.

### 2.3. Characterizations

The composition and chemical valence states of the samples were probed by X-ray photoelectron spectroscopy (XPS). Figure 3a,b show the XPS characterization of O 1s and Ni 2p<sub>3/2</sub> for different nickel oxide samples. As shown in Figure 3a, O 1s can be deconvoluted into two spectral peaks, one with a lower binding energy peak (peak 1) at near 530 eV, and another with a higher binding energy peak (peak 2) at about 532 eV, respectively. Peak 1 can be assigned to the surface lattice oxygen species O<sup>2-</sup>, while peak 2 can be assigned to the oxygen species O<sup>-</sup>, which can be attributed to the formation of an oxygen–Ni<sup>3+</sup> bond [25]. It was noted that the ratio of peak 2 to peak 1 in the *meso*-NiO sample is significantly greater than that of *bulk*-NiO, showing that the O<sup>-</sup> species of the former is significantly higher than that of the latter.

As shown in Figure 3b, Ni 2p<sub>3/2</sub> can be deconvoluted into Ni<sup>2+</sup> (855 eV) and Ni<sup>3+</sup> (856 eV) and shake-up satellite (~862 eV) for all of the samples. In the case of *meso*-NiO, the intensity of the Ni<sup>3+</sup> 2p<sub>3/2</sub> peak was much stronger than that of the Ni<sup>2+</sup> 2p<sub>3/2</sub> peak. This may be related to the particle size and the surface effect of the catalyst. *Meso*-NiO has a small particle size and a strong surface effect resulting in a relatively high peak of the binding energy spectrum. In addition, the valence and composition of Ni elements are also factors that determine the strength of the binding energy. The non-stoichiometric *meso*-NiO contains more Ni<sup>2+</sup> cation vacancies; part of Ni<sup>2+</sup> is oxidized to higher valence states to maintain electrical neutrality. Therefore, the presence of more high-valence Ni cations indicates a higher density of non-stoichiometric nickel oxide.

Figure 3c is the Raman spectra of the two samples. A Ni–O stretching vibration peak at near 500 cm<sup>-1</sup> appeared in the spectra [26]. The shoulder peak at about 375 cm<sup>-1</sup> is related to the vacancy concentration of Ni cations [27]. It can be seen from Figure 3c that the shoulder of *meso*-NiO is more obvious than that of *bulk*-NiO. Therefore, it can be concluded that the concentration of Ni<sup>3+</sup> cations or Ni vacancy in the former is greater. This result is consistent with the results of XPS characterization.

The distinct difference of active oxygen species between these two NiO can also be proved from the O<sub>2</sub>-TPD tests, as shown in Figure 3d. The desorption oxygen species below 700 °C are non-stoichiometric oxygen, which is attributed mainly to the O<sup>2-</sup> and O<sup>-</sup> species. As can be seen from Figure 3d, the amount of O<sup>-</sup> species in the *meso*-NiO sample is significantly higher than that of the *bulk*-NiO sample. This result is consistent with the results of XPS.

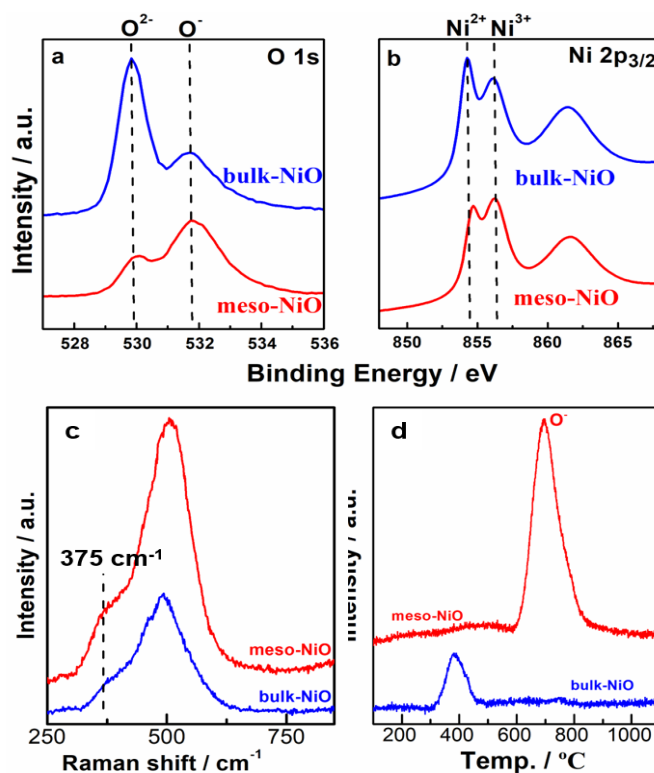


**Figure 3.** (a) O 1s for XRD, (b) Ni 2p<sub>3/2</sub> for X-ray photoelectron spectroscopy (XPS), (c) Raman, and (d) O<sub>2</sub> temperature programmed desorption (O<sub>2</sub>-TPD) characterizations of the *meso*-NiO and *bulk*-NiO catalysts.

#### 2.4. Discussion

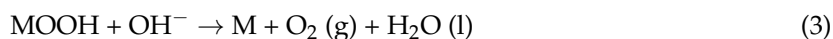
From the above results, it was concluded that the mesoporous nickel oxide exhibits a superior electrocatalytic performance compared to regular nickel oxide in the electrochemical OER reaction. These enhanced activities were beneficial from several aspects, such as geometric and electron structure effects and surface properties.

Firstly, the geometric structure, such as particle size, specific surface area, and mesopores of the catalyst, has a certain influence on the OER performance of nickel oxide. Electrocatalytic reactions commonly take place on the surface of a catalyst, which means that electrochemical performance can be strongly influenced by the geometric structure. The pore structure of mesoporous materials plays an essential role to improve the catalytic performance of the catalyst. The features of a larger surface area and pore volume formed by the aggregation of nanocrystalline NiO in *meso*-NiO are beneficial for efficient electron transfer, therefore enhancing the conductivity and improving the catalytic efficiency. Also, a large aperture can enlarge the range of reaction by promoting the full contact of the active center and reaction species and intermediates.

Secondly, the OER activity has a relationship with the type of metal oxide catalysts. An electrical double layer is formed when a metal oxide electrode is inserted into an electrolyte. Metal oxides provide a much lower charge carrier concentration compared with metals. Therefore, a large space charge layer is formed at the surface of the electrode. In general, due to the accumulation of surface pores, the potential drop in the space charge layer is negligible for the *p*-type metal oxide at anodic potentials, which is typical for OERs. In contrast, the space charge layer of the interface can cause additional obstacles to the charge carrier for an *n*-type oxide. Therefore, as a catalyst material, a *p*-type semiconducting oxide should be more suitable for OER than an *n*-type oxide [28]. NiO is a typical *p*-type oxide, which has the advantage as being an OER catalyst. For *p*-type semiconductors, the oxygen species O<sup>2-</sup>, O<sup>-</sup>, and holes (h<sup>+</sup>) will be balanced by the conversion: O<sup>2-</sup> + h<sup>+</sup> ↔ O<sup>-</sup>, and the number

of holes determines the number of  $O^-$ . Meanwhile, the as-prepared *meso*-NiO in this work is rich in nickel vacancies (holes), which will lead to the increasing of  $Ni^{3+}$  for electric neutrality. The holes derived from the vacancies of Ni cations, which depend on  $Ni^{3+}$  and other high-valent Ni ions, play an important role in the conductance. Therefore, the greater the Ni cation gap concentration, the higher density of holes, and then the better the electrical conductivity.

Thirdly, the surface properties of the NiO catalyst are also important factors affecting the electrocatalytic performance. As evidenced from the XPS,  $O_2$ -TPD, and Raman results, the *meso*-NiO is rich in  $Ni^{3+}$  and  $O^-$  species; both are electrophilic agents. It was reported that the enriched  $Ni^{3+}$  on the surface can initiate the formation of NiOOH, and was responsible for most of the redox sites acting for  $OH^-$  adsorption in alkaline solution, which was critical for enhancing OER [5]. Pfeifer proposed that the reactive species in OER over  $IrO_2$  is not solely a property of the metal; it is also intimately tied to the electronic structure of oxygen [29]. The surface electrophilic oxygen species is extremely susceptible to nucleophilic attack by water or hydroxide, which as the nucleophile donate electrons to the reactive oxygen to facilitate O–O bond formation on transition metal oxide during the OER.



Finally, the reaction mechanism could be concluded based on understanding the relationship between geometric/electron structure properties and the reaction process of the electrochemical OER process (Figure 4). In the process of OER over the NiO catalyst, there are two different paths that separate out the oxygen in an alkaline solution. One is the direct combination of Ni–O to produce oxygen (Equation (1)), and the other is to produce the intermediates (NiOOH) and then decompose to produce oxygen (Equations (2) and (3)) [26]. When a nickel metal electrode is immersed in an alkaline solution (the solution of 1 M KOH in this article), a hydrous layer can be aged in base or in vacuum to give the hydrous  $\beta$ -Ni(OH)<sub>2</sub>, which will oxidize to  $\gamma$ -NiOOH and  $\beta$ -NiOOH when the potential reaches a certain value. The latter ( $\beta$ -NiOOH) has better water oxidation activity. The electrochemical oxidation of nickel–oxide in electrochemical conditions is increased by the in situ formation of Ni(OH)<sub>2</sub>/NiOOH hydroxide/oxyhydroxide species [30,31]. The hydroperoxy (-OOH) species are the key intermediates in OER. In our case, the electrophilic  $Ni^{3+}$  and  $O^-$  species is prone to be nucleophilic attacked by  $OH^-$  in the KOH solution (Equation (4), where Ni–O\* means the electrophilic  $Ni^{3+}$  and  $O^-$  species). The formed (Ni–O–O–H)\* is also facilitated to further react with  $OH^-$  to form the product  $O_2$ . For mesoporous NiO, the high density of electrophilic  $Ni^{3+}$  and  $O^-$  species result in the enhanced OER activity.

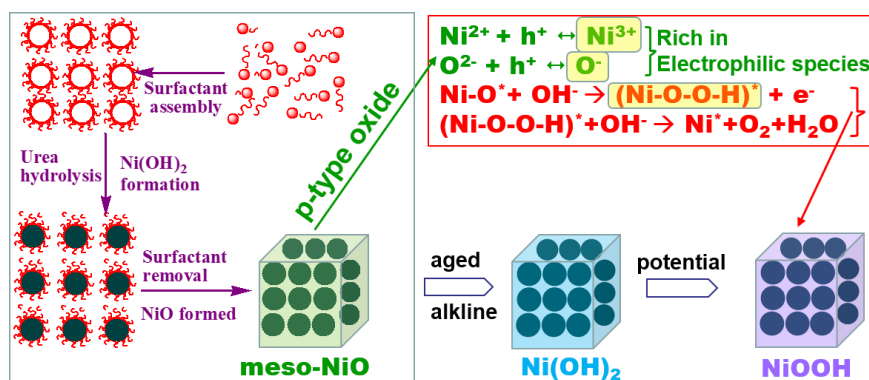


Figure 4. Representation of the fabrication process and reaction mechanism of *meso*-NiO.

### 3. Materials and Methods

#### 3.1. Materials

Materials were purchased in the grade indicated and used as received: nickel hexahydrate ( $\text{NiCl}_2 \cdot 6\text{H}_2\text{O}$ , AR, Sinopharm Chemical Reagent Co. Ltd., Shanghai, China), lauryl sodium sulfate (SDS, 95%, Energy Chemical Reagent Co. Ltd, Shanghai, China), urea ( $\text{CH}_4\text{N}_2\text{O}$ , AR, Sinopharm Chemical Reagent Co. Ltd., Shanghai, China), nickel nitrate ( $\text{Ni}(\text{NO}_3)_2$ , AR, Sinopharm Chemical Reagent Co. Ltd., Shanghai, China), citric acid ( $\text{C}_6\text{H}_8\text{O}_7\text{H}_2\text{O}$ , AR, Sinopharm Chemical Reagent Co. Ltd., Shanghai, China), caustic potash (KOH, 95%, Energy Chemical Reagent Co. Ltd., Shanghai, China), and muriate (KCl, 99.5%, Sinopharm Chemical Reagent Co. Ltd., Shanghai, China).

#### 3.2. Analytical Equipment

The equilibrium potential, stability, current density, etc. of the catalyst were determined by the electrochemical workstation (CHI660E, A17104 Chenhua Co. Ltd., Shanghai, China). All of the testing was done in a three-electrode system at 25 °C.

#### 3.3. Synthesis of Nano-Nickel Oxide

Nano-nickel oxide was synthesized by the sol-gel method [15,16]. 0.03 M  $\text{Ni}(\text{NO}_3)_2$ , and 0.03 M of citric acid was added to 50 mL of ethanol and then stirred with a glass rod until completely dissolved. The solution was placed in a water bath and heated to 80 °C to allow it to evaporate. When one-third of the solution remained, it was put in an oven and dried at 100 °C for 24 h, and then put in a muffle furnace, heated to 300 °C, and calcined for 4 h to obtain *bulk*-NiO.

#### 3.4. Synthesis of Meso-Nickel Oxide

The template method to synthesize mesoporous nickel oxide [14] takes the anionic surfactant sodium dodecyl sulfate (SDS) as a guide agent structure. Urea slowly hydrolyzes to form  $\text{NH}_3$ , which reacts with  $\text{Ni}^{2+}$  to form a  $\text{Ni}(\text{OH})_2$  precursor. In a typical process,  $\text{NiCl}_2$ , SDS, urea, and  $\text{H}_2\text{O}$  were mixed at quality ratio of 1: 2: 30: 60 and stirred at 40 °C for 1 h to obtain a clear solution. The clear solution was poured into a reaction kettle and treated at 80 °C for 20 h. The resulting material was washed several times with water and ethanol and dried overnight at 60 °C, thus obtaining a precursor  $\text{Ni}(\text{OH})_2$ . The precursor was calcined at 300 °C for 4 h to give *meso*-NiO.

#### 3.5. Characterizations

The prepared sample was characterized by XRD (Model d/Max-C, Rigaku Corporation, Tokyo Japan) [32]. The morphology of the sample was observed by SEM (LEO-1530, LEO Electron Microscope Com., Berlin, Germany) and TEM (Phillips FEI, Tecnai 30, Thermo Fisher Scientific Com., Oregon, OR, USA). The BET (AutoChem2920, Micromeritics Co. California, CA, USA) was used to test the particle size and pore volume of the sample. Raman was used to test the relationship between the Ni cation and vacancy concentration.  $\text{O}_2$ -TPD measurements were performed on a mass spectrometer and used to test the presence of oxygen species. The catalyst sample (0.2 g) was pretreated in pure oxygen flowing at 15 mL/min at the sample's calcining temperature for 1 h, and then cooled to room temperature under the oxygen flow. After the system was subsequently flushed with He to achieve a smooth baseline, the sample was heated to 900 °C at a rate of 15 °C/min in He flow (30 mL/min). The reactor exit was monitored online by a mass spectrometer. XPS was used to test the surface composition of the catalyst and the change in valence of the surface element.

#### 3.6. Electrode Preparation

The catalyst was made in a certain ratio of ink: 0.1 g of catalyst was mixed with 0.1 g of Ketjen black; then, 800  $\mu\text{L}$  of isopropanol and 200  $\mu\text{L}$  of Nafion were added and ultrasound mixed to disperse

evenly. The geometric surface area of glassy carbon electrode is 0.196 cm<sup>2</sup>. Before the electrochemical test, the working electrode was smoothed with  $\alpha$ -Al<sub>2</sub>O<sub>3</sub> with different particle sizes in a three-electrode system for testing at 25 degrees. The three-electrode system consisted of the glassy carbon electrode as a working electrode, the Pt wire as an auxiliary electrode, and Ag/AgCl as a reference electrode. The electrolyte solution was 1M KOH. We took 8  $\mu$ L of ink drops on the working electrode, dried it at room temperature, and maintained the test temperature at 25 degrees. Then, we passed O<sub>2</sub> in the 1 M of KOH for half an hour prior to testing, and then placed the oxygen tube above the liquid level to isolate the air from creating a saturated oxygen condition.

### 3.7. Electrochemical Characterization

The electrochemical capacitance measurements were determined by cyclic voltammetry (CV). The potential range was selected as the 0.1-V potential window, which had the system's open-point as the center. The test was first activated at a sweep rate of 50 mV s<sup>-1</sup> for 5 min, aiming to clean the surface of electrodes and enhance the number of oxygen-containing functional groups in the catalysts [33]. The CV test was carried out in static solution. We set five different scanning rates for scanning: 0.02 V s<sup>-1</sup>, 0.04 V s<sup>-1</sup>, 0.06 V s<sup>-1</sup>, 0.08 V s<sup>-1</sup>, and 0.1 V s<sup>-1</sup>.

The electrochemical activity for OER was assessed by linear sweep voltammetry (LSV) in the potential range of 0–0.8 V at a scan rate of 50 mV s<sup>-1</sup>. During the test, the reaction process should be continuously stirred in order to prevent the working electrode reaction bubbles from affecting the test results. The scan rate was 0.05 V s<sup>-1</sup>.

## 4. Conclusions

In summary, the *meso*-NiO composed of uniform mesopores were synthesized via the surfactant-assisted urea hydrolysis method. The as-prepared *meso*-NiO shows high-rich Ni<sup>3+</sup> cations and O<sup>-</sup> species on the surface, as well as a large surface area, which concurrently benefited the OER reaction. An overpotential of 410 mV to generate a current density of 50 mA/cm<sup>2</sup> were obtained for *meso*-NiO compared with the value of 494 mV for regular *bulk*-NiO. The outstanding electrocatalytic performance of *meso*-NiO can be attributed to the synergy of the large surface area offered by the mesoporous structure to facilitate the mass transport and surface properties with a higher density of Ni<sup>3+</sup> and O<sup>-</sup> as the main active sites on the surface. The surface electrophilic Ni<sup>3+</sup> and O<sup>-</sup> species are prone to be nucleophilic attacked by OH<sup>-</sup> in the alkaline solution to form the reactive intermediate, which is also facilitated to further react with OH<sup>-</sup> to generate oxygen. Although the performance of mesoporous nickel oxide in electrocatalysis is superior to that of nano-nickel oxide, there is still room for improvement in its performance.

**Author Contributions:** Conceptualization, L.-Z.Z.; Data curation, Z.-Y.Z., Z.C.; Funding acquisition, F.-Z.S., J.-H.L.; Investigation, X.L.; Methodology, X.-F.Z.; Supervision, J.-H.L.; Writing—original draft, X.L.; Writing—review & editing, F.-Z.S., J.-H.L.

**Funding:** This research was funded by the National Natural Science Foundation of China (No. 21773195), the Fundamental Research Funds for the Central Universities (No. 20720170030) and State Key Laboratory of New Ceramic and Fine Processing Tsinghua University (No. KF201706).

**Acknowledgments:** We thank all the graduate students for their assistance with the fieldwork.

**Conflicts of Interest:** The authors declare no conflict of interest.

## References

1. Kim, J.; Jin, H.; Oh, A.; Baik, H.; Joo, S.H.; Lee, K. Synthesis of compositionally tunable, hollow mixed metal sulphide coxniysz octahedral nanocages and their composition-dependent electrocatalytic activities for oxygen evolution reaction. *Nanoscale* **2017**, *13*, 3437–3444. [[CrossRef](#)] [[PubMed](#)]
2. Michalska-Domanska, M.; Norek, M.; Jóźwik, P.; Jankiewicz, B.; Stepniowski, W. Catalytic stability and surface analysis of microcrystalline Ni<sub>3</sub>Al thin foils in methanol decomposition. *Appl. Surf. Sci.* **2014**, *293*, 169–176. [[CrossRef](#)]

3. Tang, C.; Asiri, A.M.; Sun, X. Highly-active oxygen evolution electrocatalyzed by a Fe-doped NiSe nanoflake array electrode. *Chem. Commun.* **2016**, *52*, 4529–4532. [[CrossRef](#)] [[PubMed](#)]
4. Wang, J.; Cui, W.; Liu, Q.; Xing, Z.; Asiri, A.M.; Sun, X. Recent progress in cobalt-based heterogeneous catalysts for electrochemical water splitting. *Adv. Mater.* **2016**, *28*, 215–230. [[CrossRef](#)] [[PubMed](#)]
5. Trotochaud, L.; Ranney, J.K.; Williams, K.N.; Boettcher, S.W. Solution-cast metal oxide thin film electrocatalysts for oxygen evolution. *J. Am. Chem. Soc.* **2012**, *134*, 17253–17261. [[CrossRef](#)] [[PubMed](#)]
6. Wang, H.Y.; Hsu, Y.Y.; Chen, R.; Chan, T.S.; Chen, H.M.; Liu, B. Ni<sup>3+</sup>-induced formation of active NiOOH on the spinel Ni-Co oxide surface for efficient oxygen evolution reaction. *Adv. Energy Mater.* **2015**, *5*, 395–417. [[CrossRef](#)]
7. Matsumura, Y.; Tanaka, K.; Tode, N.; Yazawa, T.; Haruta, M. Catalytic methanol decomposition to carbon monoxide and hydrogen over nickel supported on silica. *J. Mol. Catal. A Chem.* **2000**, *152*, 157–165. [[CrossRef](#)]
8. Taguchi, A.; Schüth, F. Ordered mesoporous materials in catalysis. *Micropor. Mesopor. Mater.* **2005**, *77*, 1–45. [[CrossRef](#)]
9. Chang, J.; Park, M.; Ham, D.; Ogale, S.B.; Mane, R.S.; Han, S.H. Liquid-phase synthesized mesoporous electrochemical supercapacitors of nickel hydroxide. *Electrochim. Acta* **2008**, *53*, 5016–5021. [[CrossRef](#)]
10. Yuan, C.; Gao, B.; Su, L.; Zhang, X. Interface synthesis of mesoporous MnO<sub>2</sub> and its electrochemical capacitive behaviors. *J. Colloid Interface Sci.* **2008**, *322*, 545–550. [[CrossRef](#)] [[PubMed](#)]
11. Wang, Y.G.; Xia, Y.Y. Electrochemical capacitance characterization of NiO with ordered mesoporous structure synthesized by template SBA-15. *Electrochim. Acta* **2006**, *51*, 3223–3227. [[CrossRef](#)]
12. Xing, W.; Li, F.; Yan, Z.F.; Lu, G.Q. Synthesis and electrochemical properties of mesoporous nickel oxide. *J. Power Sources* **2004**, *134*, 324–330. [[CrossRef](#)]
13. Shaju, K.M.; Jiao, F.; Débart, A.; Bruce, P.G. Mesoporous and nanowire Co<sub>3</sub>O<sub>4</sub> as negative electrodes for rechargeable lithium batteries. *Phys. Chem. Chem. Phys.* **2007**, *9*, 1837–1842. [[CrossRef](#)] [[PubMed](#)]
14. Li, J.-H.; Wang, C.-C.; Huang, C.-J.; Sun, Y.-F.; Weng, W.-Z.; Wan, H.-L. Mesoporous nickel oxides as effective catalysts for oxidative dehydrogenation of propane to propene. *Appl. Catal. A Gen.* **2010**, *382*, 99–105. [[CrossRef](#)]
15. He, Y.; Wu, Y.; Chen, T.; Weng, W.; Wan, H. Low-temperature catalytic performance for oxidative dehydrogenation of propane on nanosized Ti(Zr)-Ni-O prepared by modified sol-gel method. *Catal. Commun.* **2006**, *7*, 268–271. [[CrossRef](#)]
16. Alberto, N.; Vigario, C.; Duarte, D.; Almeida, D.; Gonçalves, G. Characterization of graphene oxide coatings onto optical fibers for sensing applications. *Mater. Today Proc.* **2015**, *2*, 171–177. [[CrossRef](#)]
17. Schenk, A.S.; Eiben, S.; Goll, M.; Reith, L.; Kulak, A.N.; Meldrum, F.C.; Jeske, H.; Wege, C.; Ludwigs, S. Virus-directed formation of electrocatalytically active nanoparticle-based Co<sub>3</sub>O<sub>4</sub> tubes. *Nanoscale* **2017**, *9*, 6334–6345. [[CrossRef](#)] [[PubMed](#)]
18. Han, L.; Dong, C.; Zhang, C.; Gao, Y.; Zhang, J.; Gao, H.; Wang, Y.; Zhang, Z. Dealloying-directed synthesis of efficient mesoporous CoFe-based catalysts towards the oxygen evolution reaction and overall water splitting. *Nanoscale* **2017**, *9*, 16467–16475. [[CrossRef](#)] [[PubMed](#)]
19. Lyons, M.E.; Brandon, M.P. The oxygen evolution reaction on passive oxide covered transition metal electrodes in aqueous alkaline solution. Part 1-nickel. *Int. J. Electrochem. Sci.* **2008**, *3*, 1386–1424.
20. Li, W.; Gao, X.; Wang, X.; Xiong, D.; Huang, P.P.; Song, W.G.; Bao, X.; Liu, L. From water reduction to oxidation: Janus Co-Ni-P nanowires as high-efficiency and ultrastable electrocatalysts for over 3000h water splitting. *J. Power Sources* **2016**, *330*, 156–166. [[CrossRef](#)]
21. Zhou, W.; Wu, X.; Cao, X.; Huang, X.; Tan, C.; Tian, J.; Liu, H.; Wang, J.; Zhang, H. Ni<sub>3</sub>S<sub>2</sub> nanorods/Ni foam composite electrode with low overpotential for electrocatalytic oxygen evolution. *Energ. Environ. Sci.* **2013**, *6*, 2921–2924. [[CrossRef](#)]
22. Sun, H.; Zhao, Y.; Mølhave, K.; Zhang, M.; Zhang, J. Simultaneous modulation of surface composition, oxygen vacancies and assembly in hierarchical Co<sub>3</sub>O<sub>4</sub> mesoporous nanostructures for lithium storage and electrocatalytic oxygen evolution. *Nanoscale* **2017**, *9*, 14431–14441. [[CrossRef](#)] [[PubMed](#)]
23. Suen, N.T.; Hung, S.F.; Quan, Q.; Zhang, N.; Xu, Y.J.; Chen, H.M. Electrocatalysis for the oxygen evolution reaction: Recent development and future perspectives. *Chem. Soc. Rev.* **2017**, *46*, 337–365. [[CrossRef](#)] [[PubMed](#)]
24. Zhang, B.; Yu, H.L.; Ni, H.; Hu, S. Bimetallic (Fe<sub>x</sub>Ni<sub>1-x</sub>)<sub>2</sub>P nanoarrays as exceptionally efficient electrocatalysts for oxygen evolution in alkaline and neutral media. *Nano Energy* **2017**, *38*, 553–560. [[CrossRef](#)]

25. Stoyanova, M.; Konova, P.; Nikolov, P.; Naydenov, A.; Christoskova, S.; Mehandjiev, D. Alumina-supported nickel oxide for ozone decomposition and catalytic ozonation of CO and VOCs. *Chem. Eng. J.* **2006**, *122*, 41–46. [[CrossRef](#)]
26. Cordoba-Torresi, S.I. Electrochromic behavior of nickel oxide electrodes. *J. Electrochem. Soc.* **1991**, *138*, 1554–1559. [[CrossRef](#)]
27. Heracleous, E.; Lemonidou, A.A. Ni-nb-o mixed oxides as highly active and selective catalysts for ethene production via ethane oxidative dehydrogenation. Part i: Characterization and catalytic performance. *J. Catal.* **2006**, *237*, 162–174. [[CrossRef](#)]
28. Fabbri, E.; Haberer, A.; Waltar, K.; Kötz, R.; Schmidt, T.J. Developments and perspectives of oxide-based catalysts for the oxygen evolution reaction. *Catal. Sci. Technol.* **2014**, *4*, 3800–3821. [[CrossRef](#)]
29. Pfeifer, V.; Jones, T.E.; Wrabetz, S.; Massue, C.; Velasco Velez, J.J.; Arrigo, R.; Scherzer, M.; Piccinin, S.; Havecker, M.; Knop-Gericke, A. Reactive oxygen species in iridium-based oer catalysts. *Chem. Sci.* **2016**, *7*, 6791–6795. [[CrossRef](#)] [[PubMed](#)]
30. Corrigan, D.A.; Bendert, R.M. Effect of coprecipitated metal ions on the electrochemistry of nickel hydroxide thin films: Cyclic voltammetry in 1 M KOH. *J. Electrochem. Soc.* **1989**, *20*, 723–728. [[CrossRef](#)]
31. Wehrens-Dijksma, M.; Notten, P.H.L. Electrochemical quartz microbalance characterization of Ni(OH)<sub>2</sub>-based thin film electrodes. *Electrochim. Acta* **2006**, *51*, 3609–3621. [[CrossRef](#)]
32. Michalska-Domańska, M.; Józwiak, P.; Jankiewicz, B.J.; Bartosewicz, B.; Siemiaszko, D.; Stępniewski, W.J.; Bojar, Z. Study of Cyclic Ni<sub>3</sub>Al Catalyst Pretreatment Process for Uniform Carbon Nanotubes Formation and Improved Hydrogen Yield in Methanol Decomposition. *Mater. Today Proc.* **2016**, *3S*, S171–S177. [[CrossRef](#)]
33. Chen, G.F.; Ma, T.Y.; Liu, Z.Q.; Li, N.; Su, Y.Z.; Davey, K.; Qiao, S.Z. Efficient and stable bifunctional electrocatalysts Ni/NixMy (M = P, S) for overall water splitting. *Adv. Funct. Mater.* **2016**, *26*, 3314–3323. [[CrossRef](#)]



© 2018 by the authors. Licensee MDPI, Basel, Switzerland. This article is an open access article distributed under the terms and conditions of the Creative Commons Attribution (CC BY) license (<http://creativecommons.org/licenses/by/4.0/>).